Supporting Information

Defect Engineering of Ceria Nanocrystals for Enhanced Catalysis via a High-Entropy Oxide Strategy

Yifan Sun[1,2], Tao Wu[3], Zhenghong Bao[1], Jisue Moon[1], Zhennan Huang[4], Zitao Chen[4], Hao Chen[5], Meijia Li,[1] Zhenzhen Yang[1], Miaofang Chi[4], Todd J. Toops,[6] Zili Wu[1,4], De-en Jiang[3], Jue Liu[7,*], Sheng Dai[1,5,*]

[1]Chemical Sciences Division, Oak Ridge National Laboratory, Oak Ridge, Tennessee 37831, United States.
[2]Frontiers Science Center for Transformative Molecules, School of Chemistry and Chemical Engineering, Shanghai Jiao Tong University, Shanghai 200240, China.
[3]Department of Chemistry, University of California, Riverside, California 92521, United States.
[4]Center for Nanophase Materials Sciences, Oak Ridge National Laboratory, Oak Ridge, Tennessee 37831, United States.
[5]Department of Chemistry, The University of Tennessee, Knoxville, Tennessee 37996, United States.
[6]Buildings and Transportation Science Division, Oak Ridge National Laboratory, Oak Ridge, Tennessee 37831, United States.
[7]Neutron Scattering Division, Oak Ridge National Laboratory, Oak Ridge, Tennessee 37831, United States.

E-mail: dais@ornl.gov; liuj1@ornl.gov

Table of Contents **Page**

EXPERIMENTAL

Chemicals. Cerium(III) nitrate hexahydrate ($Ce(NO_3)_3 \cdot 6H_2O$, 99% trace metals basis), copper(II) nitrate trihydrate ($Cu(NO_3)_2 \cdot 3H_2O$, purum p.a., 98.0-103% (RT)), cobalt(II) nitrate hexahydrate ($Co(NO_3)_2 \cdot 6H_2O$, ACS reagent, ≥98%), nickel(II) nitrate hexahydrate ($Ni(NO_3)_2 \cdot 6H_2O$, puriss. p.a., ≥98.5% (KT)), manganese(II) nitrate tetrahydrate ($Mn(NO_3)_2 \cdot 4H_2O$, purum p.a., ≥97.0% (KT)), oleylamine (technical grade, 70%), 1-octadecene (technical grade, 90%), and white quartz (SiO_2, ≥99.995%, trace metals basis) were purchased from Sigma Aldrich. Iron(III) nitrate nonahydrate ($Fe(NO_3)_3 \cdot 9H_2O$, 99+%) was purchased from Acros Organics. Solvents, including hexane, ethanol, and acetone were of analytical grade. All chemicals were used as received without further purification.

Synthesis of transition-metal-doped CeO_2 nanocrystals. Colloidal CeO_2 and transition-metal-doped CeO_2 nanocrystals were synthesized via modifying the method reported by Lee *et al*.[1] In the colloidal synthesis of CeO_2 nanocrystals, 868 mg of $Ce(NO_3)_3 \cdot 6H_2O$ (2 mmol), 13 mL 1-octadecene (40 mmol) and 2 mL oleylamine (6 mmol) were added to a 100 mL three-neck flask at room temperature, and stirred under argon at 80 °C for 30 min to form a homogeneous solution. The mixture was then heated to 220 °C under argon. After 2h, the reaction was stopped with the heating mantle removed. After cooling down to room temperature, the products were washed five times with a 1:1 ethanol/acetone mixture and hexane for redispersion. For the transition-metal-doped CeO_2 nanocrystals, same synthetic protocol was employed with stoichiometric addition of the transition metal nitrate precursors. All the colloidal nanocrystals were then annealed in air at 500 °C for 4h to remove the surface ligands, and the obtained nanopowders were stored for subsequent characterizations and catalytic measurements.

Characterization. TEM and HRTEM images were acquired using an aberration-corrected FEI Titan S 80-300 STEM/TEM microscope equipped with a Gatan OneView camera at 300 kV. At least 100 particles were analyzed for the size-distribution analysis. HAADF-STEM images with STEM-EDS and STEM-EELS element maps were taken using a JEOL NEOARM operating at 200 kV. Powder XRD patterns were collected with a PANalytical Empyrean X-ray diffractometer equipped with Cu Kα radiation, with the operating voltage of 45 kV and current of 40 mA. Simulated XRD patterns were generated using the CrystalMaker/CrystalDiffract software package. Raman measurements with 532 nm laser were performed in a Renishaw inVia confocal microscope-based Raman spectrometer. Raman measurements with 325 nm (HeCd laser, Melles Griot) were performed on a multiwavelength Raman system, where the spectra were collected with a customized ellipsoidal mirror and directed by a fiber optics bundle to the spectrograph stage of a triple Raman spectrometer (Princeton InstrumentsActon Trivista 555). Edge filters (Semrock) were used in front of the UV-vis fiber optic bundle (Princeton Instruments) to block the laser irradiation. A UV-enhanced liquid N_2-cooled CCD detector (Princeton Instrument) was employed for signal detection. Inductively coupled plasma-atomic emission spectroscopy (ICP-AES) was performed using an Optima 2100 DV spectrometer (PerkinElmer Corporation). X-ray photoelectron spectroscopy (XPS) measurements were performed with a PHI 3056 spectrometer equipped with an Al anode source operated at 15 kV with an applied

power of 350 W and a pass energy of 93.5 eV. Samples were mounted on foil, and peaks were charge referenced to the CH_x peak in the carbon 1s spectra at 284.8 eV. Thermal gravimetric analysis (TGA) data were obtained with TA Instrument TA Q50 under air. Fourier transform infrared (FTIR) data were obtained with PerkinElmer Frontier IR system coupled with universal ATR sampling accessory. Nitrogen adsorption analysis was performed at 77 K with TriStar 3000, and surface area was estimated using the Brunauer, Emmett and Teller (BET) equation.[2]

XAS measurements. XAS measurements were performed at the beamline 10-ID-B of the Advanced Photon Source at Argonne National Laboratory.[3] Spectra were collected at Ce L-III edge (eV) in transmission mode with vanadium foil as the reference. Cu K edge (eV), Co K edge (eV) and Fe K edge (eV) were measured in fluorescence mode with corresponding metal foils as the reference for energy calibration as well as data analysis. The X-ray beam was monochromatized by a Si (111) monochromator. The incident beam intensity (I_0), transmitted beam intensity (I_t), fluorescence intensity (I_f) and reference (I_{ref}) were all measured by 20 cm ionization chambers. All spectra were collected at room temperature. Samples were centered on the beam and 10 scans were collected for each sample. Data were processed and analyzed using the Athena and Artemis program of the IFEFFIT package based on FEFF 6.[4] Data were rebinned with grids of 10 eV, 0.5 eV, and 0.05 eV for the pre-edge, XANES, EXAFS region, respectively. The absorption energy (E_0) was determined based on the first derivative of the edge. Reference foil data were aligned to the first zero-crossing of the second derivative of the normalized μ(E) data, which was calibrated to the literature E_0 for the Cu edge (8978.9 eV). All the data were initially fitted with k-weighing of 1, 2 and 3, and then finalized with k^2-weighting in R-space. A fit of the metal foil standard was used to determine S_0^2 for the samples. Structural parameters were determined by the fits including the degeneracy of the scattering path (N_{degen}), the change in R_{eff} (ΔR_i), the mean square relative displacement of the scattering element ($\Delta\sigma^2_i$), and the energy shift of the photoelectron (ΔE_0). For each fit, the number of independent points was not permitted to exceed 2/3 the number of variables, in keeping with the Nyquist criterion.[5]

Neutron Total Scattering Measurements. Neutron diffraction and PDF data were collected at the NOMAD beamline at the Spallation Neutron Source, Oak Ridge National Laboratory. About 200 mg of the ceria-based nanocrystals were loaded into 3 mm quartz capillaries, and four 24 min scans were collected for each sample and then summed together to improve the statistics of the data. Signal from the empty quartz capillary measurement was subtracted as background and the obtained data were normalized by the scattering intensity from a 6 mm vanadium rod to correct for detector efficiencies. Rietveld refinement and small-box least square PDF method was applied to analyze the neutron diffraction and total scattering data, respectively. A Q_{max} cut-off of 28 $Å^{-1}$ was adopted for all four samples during Fourier transform of the S(Q) to the reduced PDF G(r). No absorption correction was applied due to the small absorption cross sections associated with cerium and oxygen atoms. Ceria crystallizes in a fluorite structure with the space group of *F*m-3m, where each cerium ion is coordinated by eight oxygen ions to form a CeO_8 cube, and each oxygen ion is bonded to four cerium ions, forming an OCe_4 tetrahedron (Figure S16). The interstitial octahedral sites formed by six cerium ions are vacant and thus allow the formation of potential Frenkel-type oxygen defects, *i.e.*, the oxygen ion partially

moving from the original OCe_4 tetrahedral site to the interstitial OCe_6 octahedral site.[6,7] It is also possible that oxygen on the original tetrahedral site displaces along the <111> directions, forming partially degenerate sites and form another type of Frenkel defect sites. The original oxygen site has the degeneracy of 8, while the interstitial octahedral site has a degeneracy of 24 (with site splitting) and the split tetrahedral oxygen site has a degeneracy of 32. In our study, we found that splitting of the oxygen tetrahedral site dominates while the occupancies refined on the interstitial OCe_6 octahedral site is very limited (less than 1%). We also took the case where the oxygen anions displace along the <110> directions into consideration, which did not yield satisfactory fitting results. Therefore, only the interstitial octahedral site (with site splitting and a degeneracy of 32) was incorporated into the model. Structure refinements were carried out using the TOPAS v6 software.[8] For the Rietveld refinement of the Bragg diffraction data (Table S6), time-of-flight (TOF) data were converted to d-spacing data using the conventional second order polynomial TOF = *ZERO* + *DIFC**d + *DIFA**d^2, where *ZERO* is a constant, *DIFC* is the diffractometer constant and *DIFA* is an empirical term to correct for sample displacement and absorption caused peak shift. ZERO and DIFC were determined from the refinement of a standard NIST Si-640e data set and held fixed, while DIFA was allowed to vary during refinements to account for the sample displacements. A back-to-back exponential function convoluted with a symmetrical Gaussian function was used to describe the peak profile. For PDF data analysis, the instrument constants Q_{broad} and Q_{damp} were determined from the refinement of a Si-640e standard to be 0.19 $Å^{-1}$ and 0.21 $Å^{-1}$, separately. The analytical spherical shape function (or envelope function) was used to quantify the shape and size effect for the CeO_2 nanocrystals, and more details about this method can be found in previous studies.[9,10] Isotropic atomic displacement parameters were used for both Rietveld and PDF refinements. Secondary phases as observed in the Bragg diffraction results that were attributed to the rocksalt HEO domains, were incorporated for the structure refinements of CuCoFeNiMn-CeO_2 with PDF analysis. Surface Ce_7O_{12}-like phase was also incorporated in the final structure refinements for all the four samples, where substantial amounts of the surface phase were found in CuCoFeNiMn-CeO_2 (Figure S19 and S20). The lattice parameters refined from PDF differs slightly from that obtained using Rietveld refinement, as PDF contains both dynamic (e.g., phonon, or lattice vibration) and static scattering information, while Rietveld refinement only uses the static scattering (or time-average) data.[11]

Theoretical calculations. All first-principles calculations were carried out using the projector augmented wave (PAW) method implemented in the Vienna ab initio simulation package (VASP).[12–15] The generalized gradient approximation (GGA) in the Perdew−Burke−Ernzerhof (PBE) form was used for the exchange-correlation functional.[16,17] The kinetic energy cut-off was set to 500 eV for the planewaves with spin polarization included. The lattice constants and atomic positions were both fully relaxed until the total energy and residual force on atoms converged to 10^{-5} eV and 0.01 eV $Å^{-1}$, respectively. To account for on-site Coulombic interactions of the electrons in the transition metal atoms, we employed the DFT+U formalism[18] with U = 3.32, 5.30, 3.90 and 6.20 eV for Co, Fe, Mn and Ni, respectively, which are based on the parameters used in Materials Project.[19] The U value of Ce was set to be 4.00 eV based on the previous study.[20] The 4×4 supercell was chosen for the slab model with three CeO_2 layers

(9 atomic layers). Periodic boundary conditions were imposed on these unit cells in terms of the (111) surface direction, and a vacuum layer at least 10 Å thick was used to avoid the interaction between the top and bottom surfaces. For geometry optimization, the top one CeO_2 layer was fully relaxed as the surface and the rest two layers were fixed as the bulk counterpart. Owing to the large size of the slabs studied here, the Brillouin zone was sampled using a Γ-centered grid with a 2×2×1 k-point mesh for all the slabs. COHP analysis of the surface Ce─O bond was obtained from the Local Orbital Basis Suite Toward Electronic-Structure Reconstruction (LOBSTER) program.[21,22] The oxygen vacancy formation energy (E_{vac}) for the $MCe_{47}O_{96}$ model (M = Cu, Co, Fe, Mn and Ni) was determined by the difference in energy of the slabs:
$E_{vac} = E(MCe_{47}O_{95}) + 1/2E(O_2) - E(MCe_{47}O_{96})$

Catalytic measurements. CO oxidation was performed using the Altamira Instruments system (uBenchCAT) with the catalysts loaded in a fixed-bed reactor (U-type quartz tube) with inner diameter of 4 mm at atmospheric pressure. 20 mg of the ceria-based catalyst was diluted with 200 mg white quartz, and then loaded in the reactor with quartz wool as support. The loaded catalyst was pretreated with 20 mL min^{-1} 10% O_2 balanced with Ar at 300 °C to remove gas and moisture adsorbed on the surface, and then naturally cooled down to room temperature (20 °C). The feed gas of 1% CO balanced with dry air passed though the catalyst bed at a flow rate of 12 mL min^{-1}. The temperature was increased with a ramping rate of 0.5 °C min^{-1}, and data point was obtained for every 10 min that corresponds to a 5 °C temperature interval. The reactants and products were analyzed using an Agilent 7820 gas chromatograph (GC) equipped with a thermal conductivity detector and a ShinCarbon ST column. For kinetic studies, the conversion percentage was maintained below 15% by controlling the reaction temperature, and the reaction rate was determined based on the average steady-state reaction rates in 1 h. TPOIE experiments were performed with an AMI-200 apparatus, where 50 mg of sample was loaded in a U-type quartz with quartz wool as support. The loaded sample was pretreated in a gas flow of 5% O_2 balanced with Ar (30 mL min^{-1}) at 500 °C for 30 min to remove the adsorbed impurities on the surface. After the pretreatment process, the sample was then cooled to 25 °C and then flowed with He (30 mL min^{-1}) to remove the surface-adsorbed oxygen molecules. Then 1% $^{18}O_2$ balanced with He (30 mL min^{-1}) was introduced to the samples, which was further heated to 800 °C with the ramp rate of 10 °C min^{-1}. The evolution of the gas phase was monitored by analyzing the composition using the mass spectrometer (Blazers Instruments, GSD-300), where the species with the m/z value of 32, 34 and 36 were recorded as $^{16}O_2$, $^{16}O^{18}O$ and $^{18}O_2$, respectively. After cooling down to 25 °C, TPD experiments were conducted to make sure the evolution of the oxygen isotope signals come from the exchange instead of desorption process. CO-TPR experiments were performed with an AutoChem II 2920 apparatus, where 50 mg of sample was loaded in a U-type quartz with quartz wool as support. The loaded sample was pretreated in a gas flow of 5% O_2 balanced with Ar (30 mL min^{-1}) at 500 °C for 30 min to remove the adsorbed impurities on the surface. After the pretreatment process, the sample was then cooled to 25 °C and then reduced in a flow of 1% CO balanced with He (30 mL min^{-1}) from 25 to 800 °C with the ramp rate of 10 °C min^{-1}. The CO consumption was monitored by analyzing the composition using the mass spectrometer (Blazers Instruments, GSD-300), where the species with the m/z value of 4, 18, 28, 32 and 44 were recorded as He, H_2O, CO, O_2 and CO_2,

respectively, and quantified using Gaussian peak fittings. For catalytic measurements with simulated exhaust streams, a custom fixed-bed reactor was used.[23] The catalyst was packed into a 6 mm (i.d.) quartz tube and then supported by quartz wool. A model diesel exhaust feed consisting of 0.2% CO, 0.01% NO, 0.083% C_2H_4, 0.033% C_3H_6, 0.11% C_3H_8, 6.0% CO_2, 12.0% O_2 and 6.0% H_2O balanced with Ar was used to evaluate the catalysts. A flow reactor with 111 mg of catalyst and a GHSV of 200000 h^{-1} was heated to 450 °C as a pretreatment, and then evaluated for three repeated cycles. The gas exiting the reactor was analyzed by mass spectrometry (SRS RGA100), gas chromatography (Agilent 490 Micro GC).

SUPPLEMENTARY TABLES

Table S1 Surface area of the transition-metal-substituted CeO_2 samples after annealing.

Sample	Surface Area (m^2 g^{-1})
CeO_2	72
Cu-CeO_2	89
CuCo-CeO_2	120
CuCoFeNiMn-CeO_2	104
CoFeNiMn-CeO_2	134
CoMn-CeO_2	127

Table S2 Transition metal concentrations in Cu-CeO_2, CuCo-CeO_2 and CuCoFeNiMn-CeO_2 quantified by ICP-AES.

Sample	Atomic Percentages
Cu-CeO_2	Cu: 2.5%
CuCo-CeO_2	Cu: 2.7%; Co: 5.8%
CuCoFeNiMn-CeO_2	Cu: 3.4%; Co: 3.7%; Fe: 4.8%; Ni: 3.4%; Mn: 4.9%
CuO_x-CeO_2	Cu: 22.0%

Table S3 Raman frequencies of the F_{2g}, D and 2LO mode of the transition-metal-substituted nanocrystals with the excitation wavelength of 325 nm. The I_D/I_{F2g} intensity ratio is calculated based on the Lorentzian fitting of the Raman peaks.

Sample	Position of F_{2g} / cm^{-1}	Position of D / cm^{-1}	Position of 2LO / cm^{-1}	I_D/I_{F2g}
CeO_2	467	599	1188	1.81
Cu-CeO_2	467	599	1187	1.99
CuCo-CeO_2	467	600	1188	2.08
CuCoFeNiMn-CeO_2	466	604	1193	2.86

Table S4 Raman frequencies of the F_{2g} and D mode of the transition-metal-substituted nanocrystals with the excitation wavelength of 532 nm. The I_D/I_{F2g} intensity ratio is calculated based on the Lorentzian fitting of the Raman peaks.

Sample	Position of F_{2g} / cm^{-1}	Position of D / cm^{-1}	I_D/I_{F2g}
CeO_2	464	N/A	≈0
Cu-CeO_2	465	600	0.06
CuCo-CeO_2	464	592	0.54
CuCoFeNiMn-CeO_2	460	600	1.65

Table S5 Fitting parameters of the Cu K-edge EXAFS for Cu-CeO_2, CuCo-CeO_2 and CuCoFeNiMn-CeO_2, and M represents Cu, Co, Fe, Ni or Mn.

Sample	Δ E_0 / eV	R-factor
Cu-CeO_2	–6.7(0.64)	0.006
CuCo-CeO_2	–4.66(1.15)	0.009
CuCoFeNiMn-CeO_2	–5.2(0.53)	0.027

	Cu–O			Cu–M			Cu–Ce		
Sample	CN	R / Å	Δσ² / Å²	CN	R / Å	Δσ² / Å²	CN	R / Å	Δσ² / Å²
Cu-CeO_2	3.7	1.928	0.008				3.0	3.258	0.009
	(0.29)	(0.003)	(0.001)				(0.39)	(0.009)	(0.005)
CuCo-CeO_2	2.8	1.945	0.003	0.3	2.878	0.008			
	(0.17)	(0.003)	(0.0008)	(0.10)	(0.008)	(0.005)			
CuCoFeNiMn-CeO_2	2.7	1.927	0.004	0.9	2.925	0.008			
	(0.27)	(0.005)	(0.001)	(0.43)	(0.006)	(0.006)			

Table S6 Rietveld refinement of the neutron diffraction data. Rocksalt HEOs were considered for the fitting processes of CuCo-CeO_2 and CuCoFeNiMn-CeO_2.[24] We assume the lattice parameter of the four samples remains the same upon transition metal incorporation. Surface strain and size effects in nanocrystals may induce the minimal differences of lattice parameters.[26]

Sample	R_{wp} / %	G_{of}	Lattice Parameter / Å
CeO_2	1.19	1.73	5.4112(1)
Cu-CeO_2	1.43	1.27	5.4126(2)
CuCo-CeO_2	1.14	1.28	5.4108(2)
CuCoFeNiMn-CeO_2	1.53	1.14	5.4083(4)

Table S7 Results of intermediate-range (0.5–40 Å) PDF analysis. Rocksalt HEOs were considered for the fitting processes of Cu-CeO_2, CuCo-CeO_2 and CuCoFeNiMn-CeO_2.[24] The interstitial oxygen defects were considered for the displacement along the <111> direction (the x coordination of O2 is off from 0.25).

Sample	R_{wp} / %	Lattice Parameter / Å	Frenkel ($4 \times occ._{O2}$)	xO2	Beq.Ce /Å^2	Beq.O /Å^2
CeO_2	9.9	5.4151(3)	0.093(13)	0.2810(16)	0.37(3)	0.58(4)
Cu-CeO_2	11.8	5.4173(4)	0.120(16)	0.2793(14)	0.48(4)	0.59(5)
CuCo-CeO_2	14.4	5.4141(5)	0.136(22)	0.2787(17)	0.46(5)	0.60(6)
CuCoFeNiMn-CeO_2	15.5	5.4167(6)	0.131(17)	0.2847(23)	0.49(6)	0.68(7)

Table S8 Results of short-range (0.5–10 Å) PDF analysis. Rocksalt HEOs and surface Ce_7O_{12}-like phase were considered for the fitting processes of Cu-CeO_2, CuCo-CeO_2 and CuCoFeNiMn-CeO_2.[23] The surface Ce_7O_{12}-like phase was also incorporated for the fitting of pristine CeO_2.[25] The interstitial oxygen defects were considered for the displacement along the <111> direction (the x coordination of O2 is off from 0.25).

Sample	R_{wp} / %	Lattice Parameter / Å	Frenkel ($4 \times occ._{O2}$)	xO2	Beq.Ce /Å^2	Beq.O /Å^2
CeO_2	9.8	5.4151(3)	0.056(15)	0.2812(16)	0.36(3)	0.62(4)
Cu-CeO_2	11.6	5.4173(4)	0.115(17)	0.2789(14)	0.49(4)	0.60(5)
CuCo-CeO_2	14.1	5.4142(5)	0.126(22)	0.2827(18)	0.43(5)	0.67(6)
CuCoFeNiMn-CeO_2	12.3	5.4117(6)	0.136(17)	0.2804(19)	0.47(6)	0.68(7)

SUPPLEMENTARY FIGURES

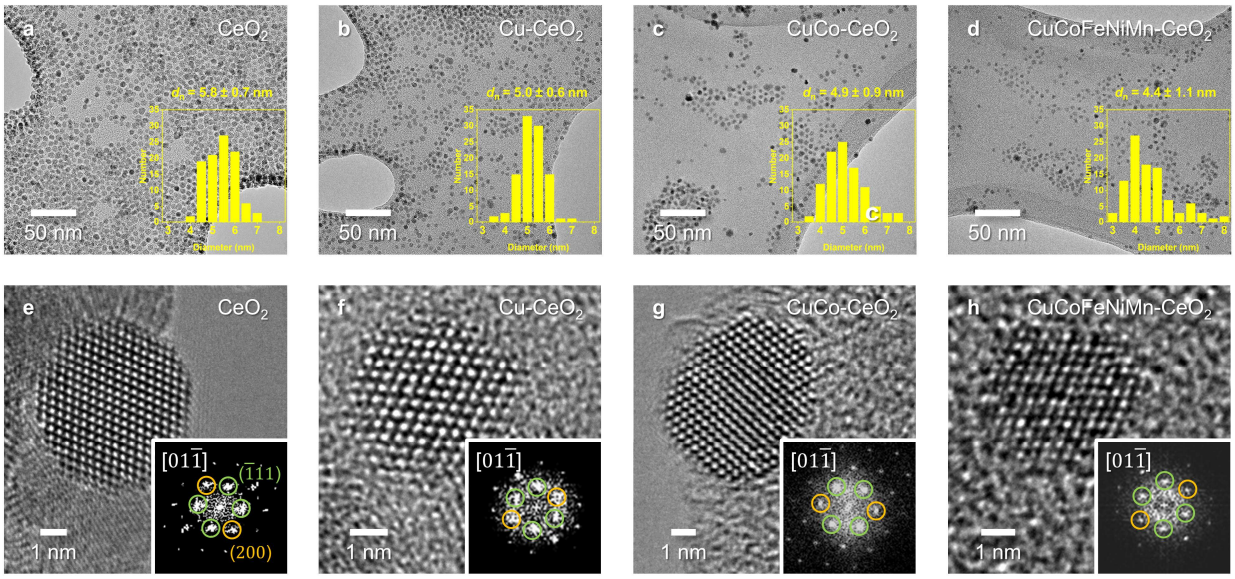

Figure S1. Low-resolution TEM images of the colloidal (a) CeO_2, (b) Cu-CeO_2, (c) CuCo-CeO_2, and (d) CuCoFeNiMn-CeO_2 nanocrystals with the corresponding size-distribution histogram. At least 100 particles were analyzed for the size-distribution analysis. High-resolution TEM images of the colloidal (e) CeO_2, (f) Cu-CeO_2, (g) CuCo-CeO_2, and (h) CuCoFeNiMn-CeO_2 nanocrystals. The diffraction patterns corresponding to the terminated {111} and {200} facets are highlighted using green and yellow circles, respectively.

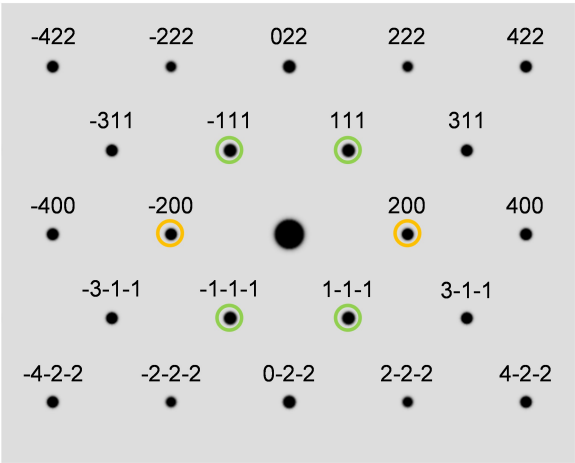

Figure S2. Simulated FFT pattern of CeO_2 viewing from the [110] direction, with the {111} and {200} diffraction spots being highlighted using green and yellow circles, respectively.

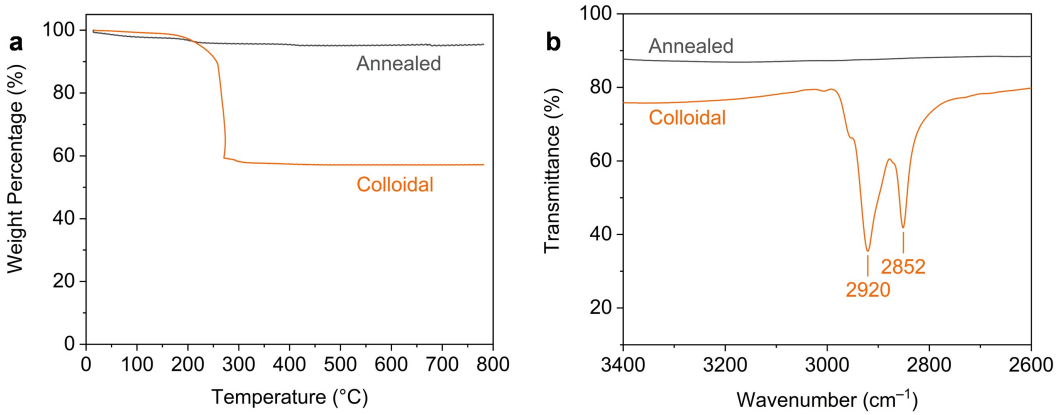

Figure S3. (a) TGA and (b) FTIR-ATR data of the colloidal and annealed CeO_2 nanocrystals, indicating the surface organic ligands are removed after the annealing process in air. The noted peaks (2852 and 2920 cm^{-1}) correspond to the C–H stretches from the surface organic ligands in the as-synthesized colloidal CeO_2 nanocrystals.[27]

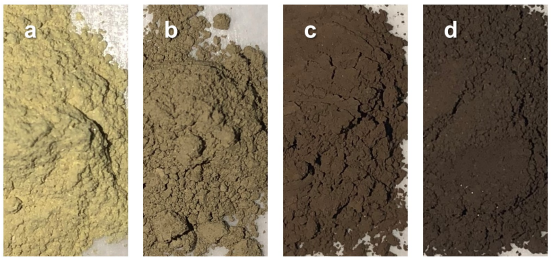

Figure S4. Pictures of the annealed (a) CeO_2, (b) Cu-CeO_2, (c) CuCo-CeO_2, and (d) CuCoFeNiMn-CeO_2 nanopowders.

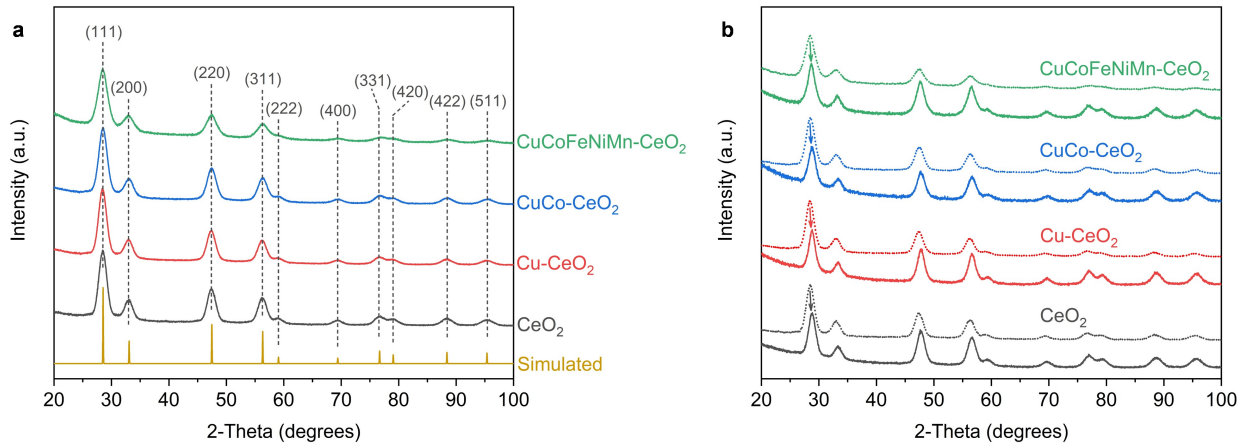

Figure S5. (a) XRD patterns of the colloidal transition-metal-substituted CeO_2 nanocrystals with reference pattern for bulk CeO_2 for comparison.[28] (b) Comparison of the XRD patterns for the colloidal and annealed CeO_2-based samples, and the shift of the XRD peaks are highlighted by arrows. The peak shift towards higher angles is mainly due to the release of surface strain during removal of the capped organic ligands.

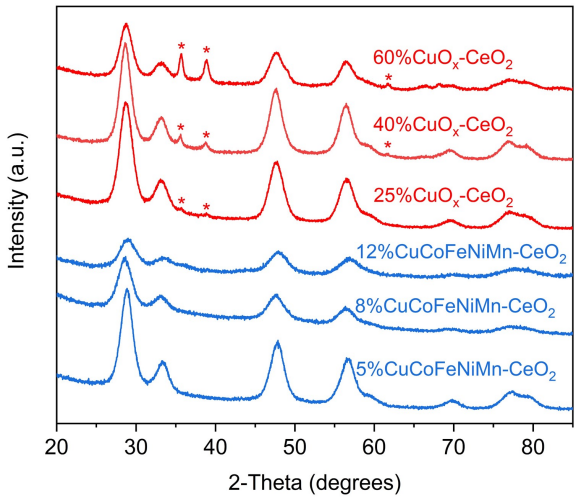

Figure S6. XRD patterns of the CuCoFeNiMn-CeO_2 and CuO_x-CeO_2 samples with the same total transition metal concentrations, showing a higher tolerance for the transition metal species through multi-cation substitution. The diffraction peaks corresponding to CuO are highlighted with asterisk signs. The broadening of the diffraction peaks for CuCoFeNiMn-CeO_2 suggests that as more transition metals are incorporated, the CeO_2 domain size becomes smaller, potentially due to the surface capping effects of the transition metal oleates.

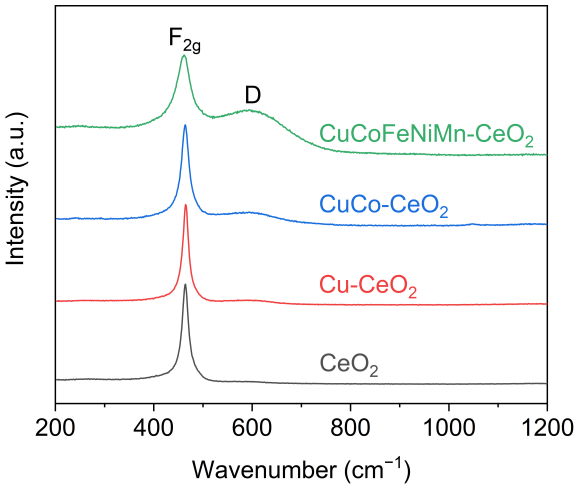

Figure S7. Raman spectra of the transition-metal-substituted CeO_2 samples with the excitation wavelength of 532 nm. The positions of the F_{2g} and D modes, as well as the I_D/I_{F2g} intensity ratio based on Lorentzian fitting are listed in Table S4 for comparison.

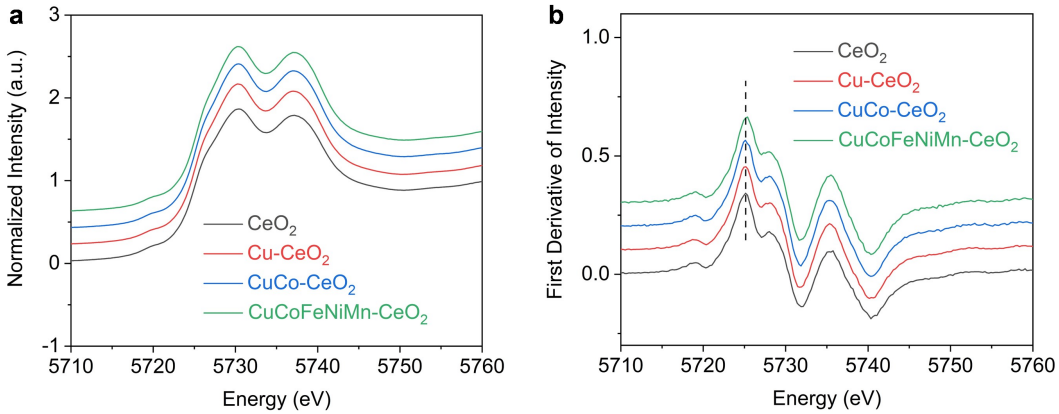

Figure S8. (a) Ce L_{III}-edge XAS spectra of the transition-metal-substituted CeO_2 samples. (b) First derivative of the adsorption spectra of the Ce L_{III}-edge, showing the energetic features of Ce remain almost the same along with transition-metal-substitution.

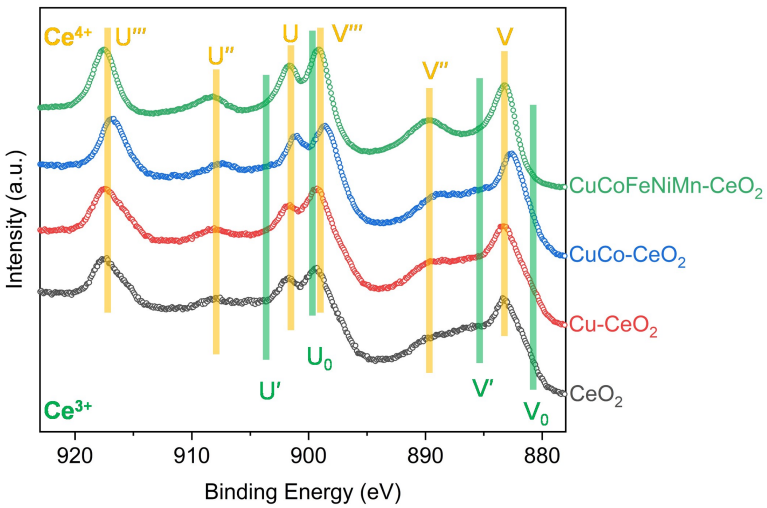

Figure S9. XPS spectra of the transition-metal-substituted CeO_2 samples. The characteristic features originating from Ce^{3+} and Ce^{4+} are highlighted with the lines in green and yellow, respectively. It is worth mentioning that the small size of the nanoparticles (~5 nm) is comparable to the probing depth (~3–8 nm), which makes XPS more like a bulk technique like XAS rather than a surface-sensitive one.

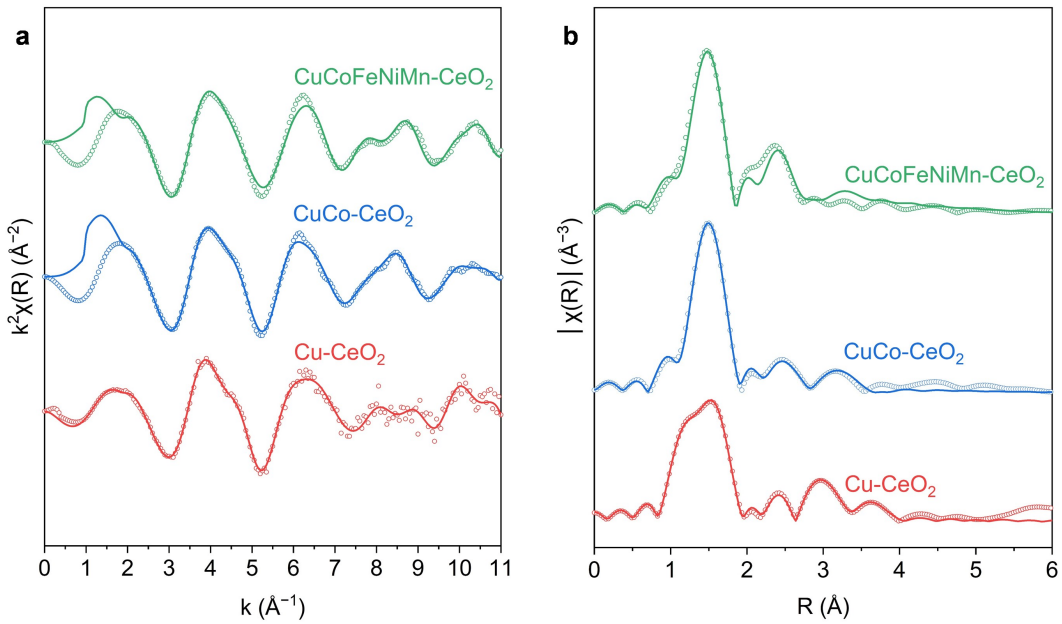

Figure S10. Cu K-edge EXAFS spectra in (a) k-space and (b) R-space for Cu-CeO_2, CuCo-CeO_2 and CuCoFeNiMn-CeO_2. Experimental and fitted data were plotted with hollow circles and solid lines, respectively. Fitting was conducted in the window with the R range of 1–5 Å and k range of 2–11 $Å^{-1}$, with the results shown in Table S5.

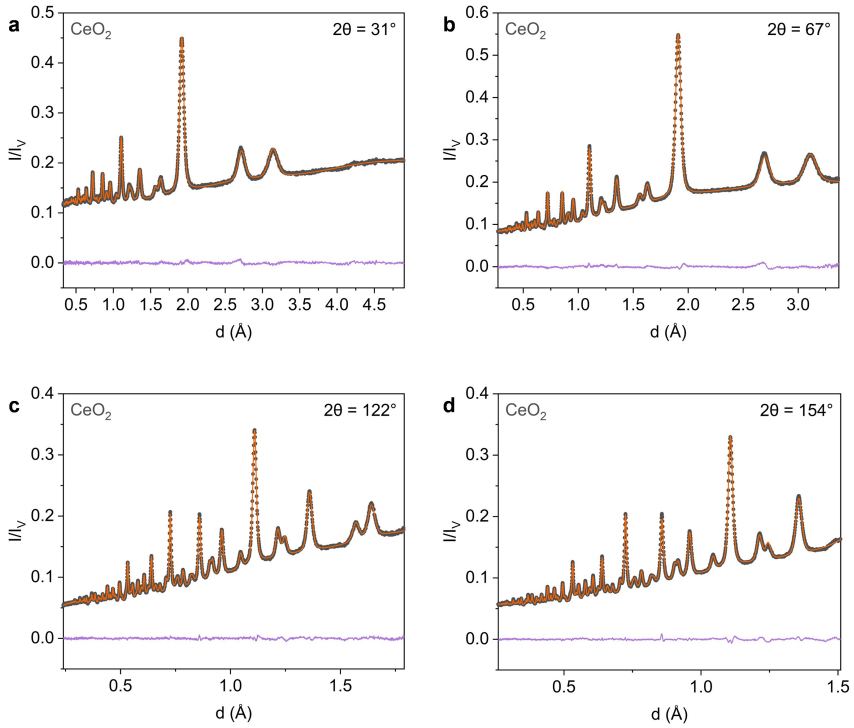

Figure S11. Rietveld refinements of the structure of the CeO_2 nanocrystals using the neutron Bragg diffraction.

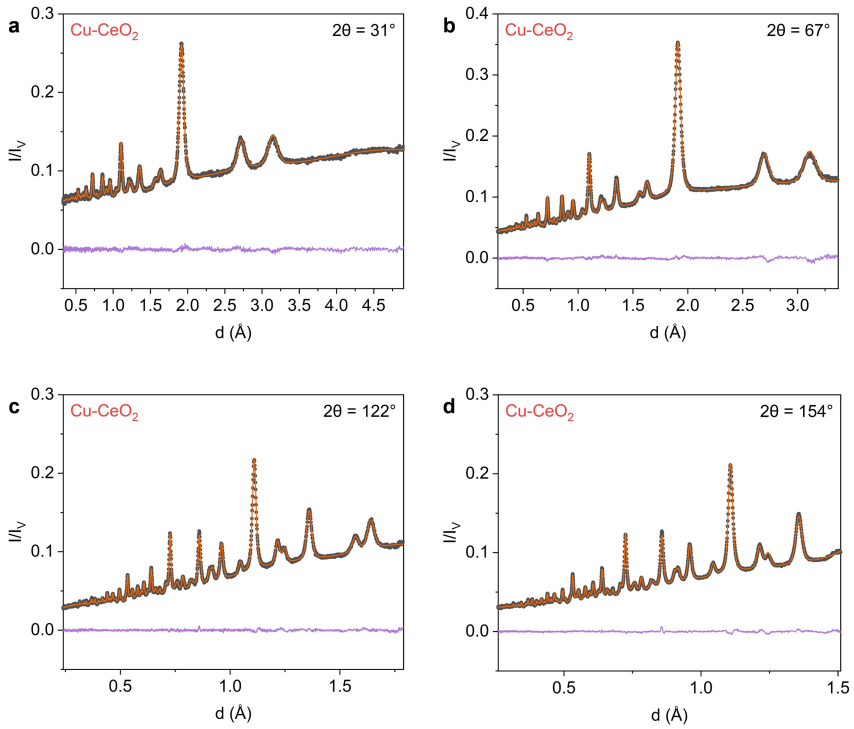

Figure S12. Rietveld refinements of the structure of the Cu-CeO_2 nanocrystals using the neutron Bragg diffraction.

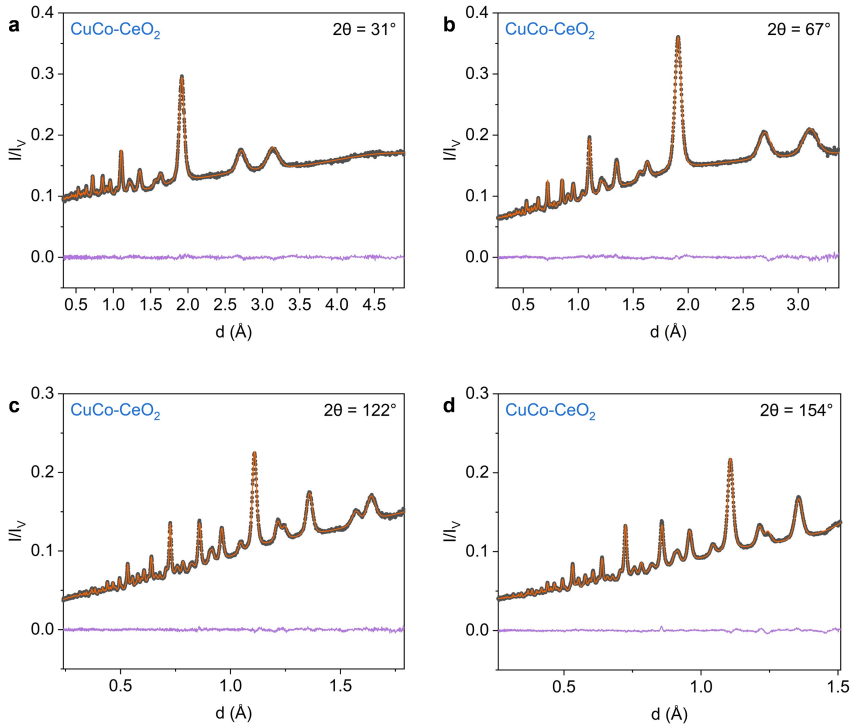

Figure S13. Rietveld refinements of the structure of the CuCo-CeO_2 nanocrystals using the neutron Bragg diffraction.

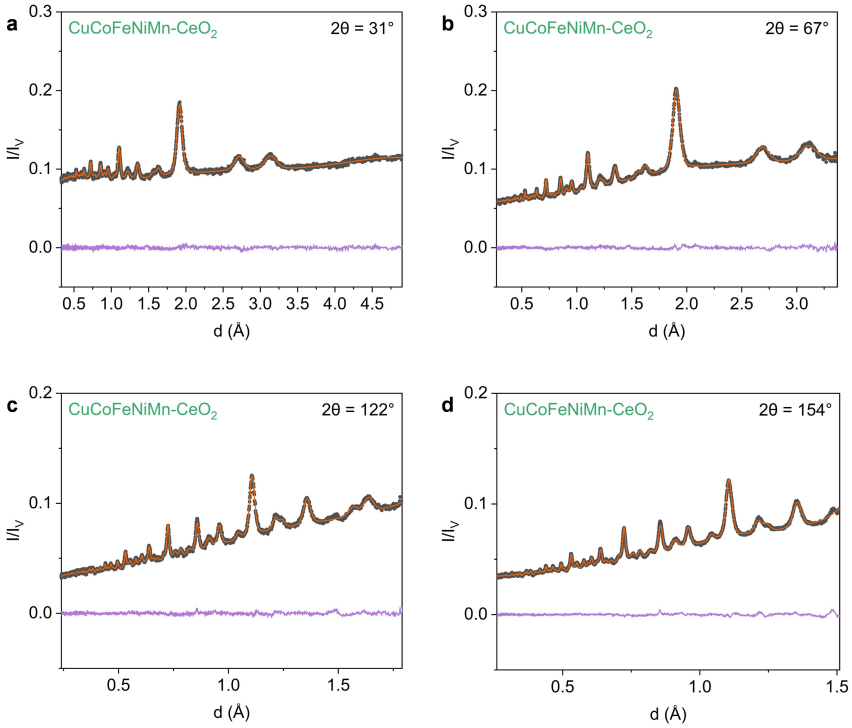

Figure S14. Rietveld refinements of the structure of the CuCoFeNiMn-CeO_2 nanocrystals using the neutron Bragg diffraction.

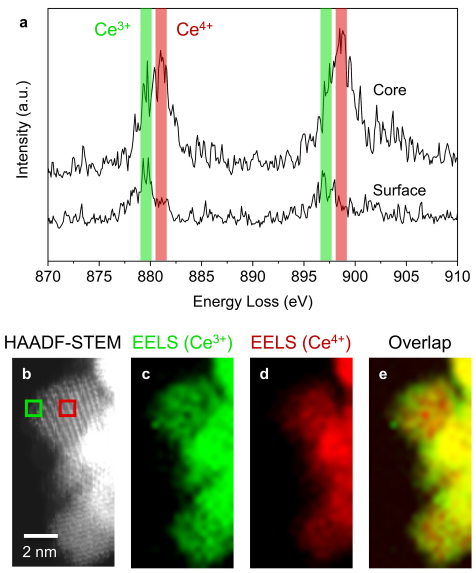

Figure S15. (a) Ce $M_{4,5}$ EELS spectra corresponding to the Ce^{3+}-rich surface and Ce^{4+}-rich core area of the CuCoFeNiMn-CeO_2 nanocrystals as highlighted in (b). (b) HAADF-STEM image, EELS elemental maps of (c) Ce^{3+} and (d) Ce^{4+}, as well as the corresponding Ce^{3+} and Ce^{4+} signal overlaps of the CuCoFeNiMn-CeO_2 nanocrystals.

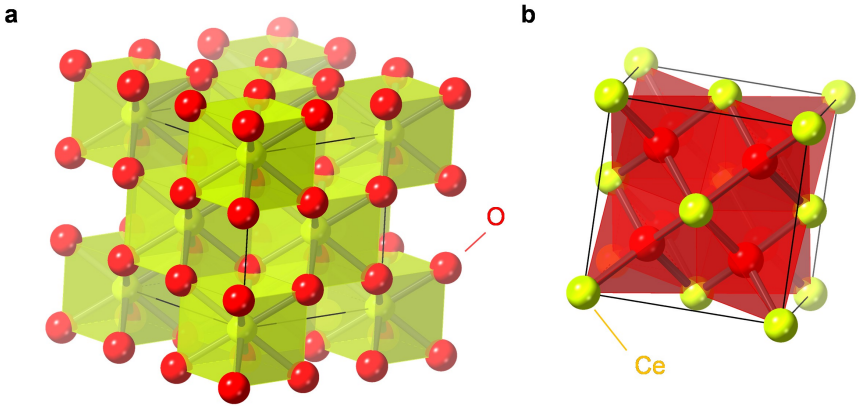

Figure S16. Schematics showing the (a) CeO8 cubes and (b) OCe4 tetrahedrons in the fluorite structure of CeO_2.

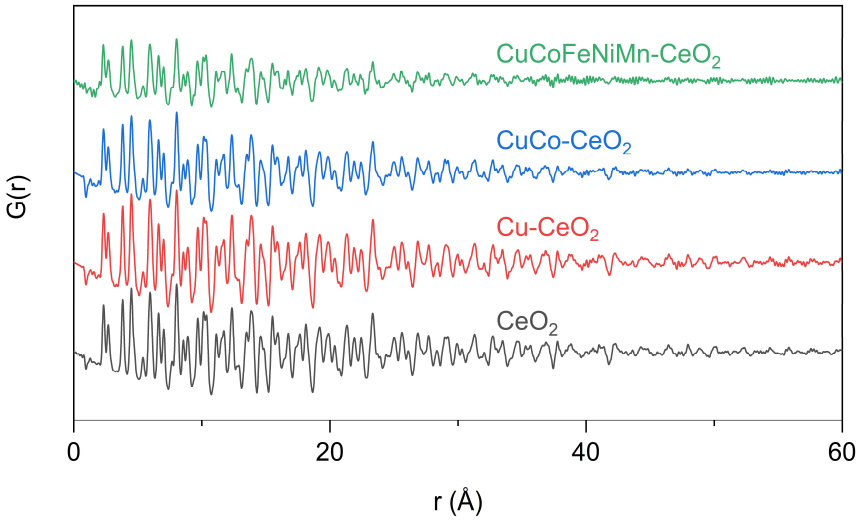

Figure S17. Neutron total scattering data of CeO_2, Cu-CeO_2, CuCo-CeO_2 and CuCoFeNiMn-CeO_2.

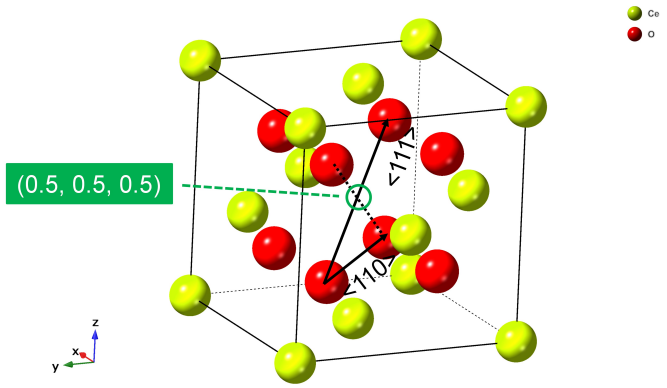

Figure S18. Schematic showing the interstitial oxygen defects in CeO_2 displaced along the <110> and <111> directions, as well as the displaced oxygen anions occupy the exact vacant octahedral sites.

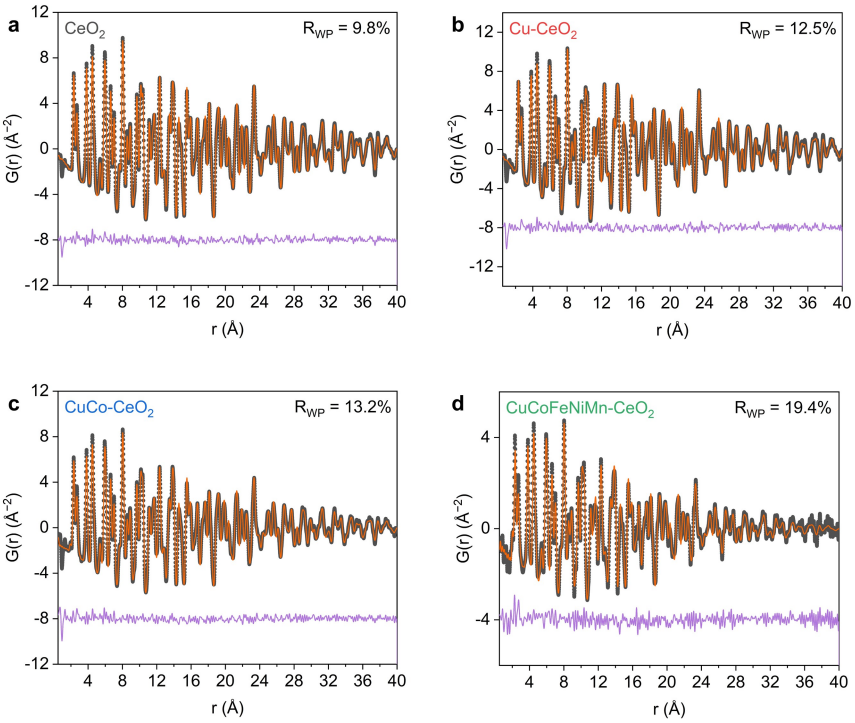

Figure S19. Intermediate-range (0.5–40 Å) PDF analysis of (a) CeO_2, (b) Cu-CeO_2, (c) CuCo-CeO_2 and (d) CuCoFeNiMn-CeO_2 based on the fluorite structure model (Table S7). The negative peak at ~1 Å is due to the surface-adsorbed hydroxyl groups (–OH).

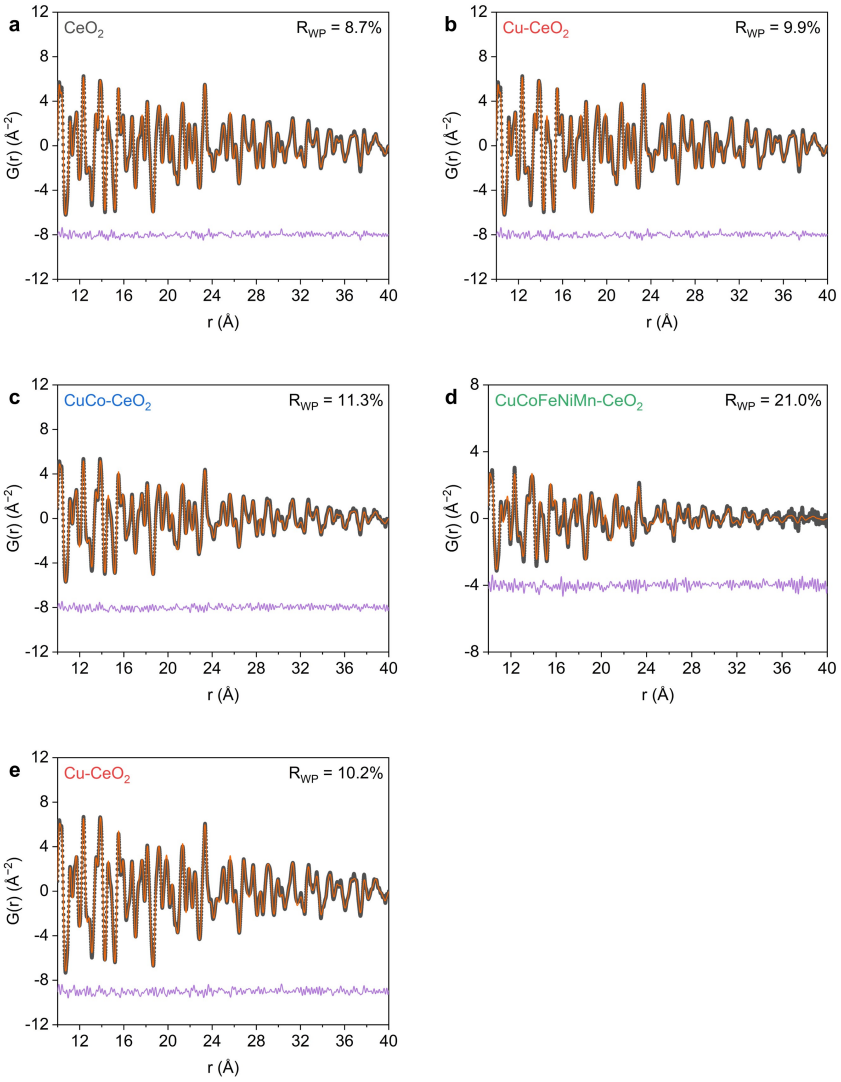

Figure S20. Intermediate-range (10–40 Å) PDF analysis of (a) CeO_2, (b) Cu-CeO_2, (c) CuCo-CeO_2 and (d) CuCoFeNiMn-CeO_2 based on the fluorite structure model. The overall improved fitting results compared with the data in Figure S19 indicates the difference mainly comes from the local structures within 10 Å, which are ascribed to the surface structures on ceria. (e) Intermediate-range (10–40 Å) PDF analysis of Cu-CeO_2 based on the fluorite structure model without taking interstitial oxygen defects into consideration. The inferior fitting results suggest the significance of interstitial oxygen defects in intermediate-range PDF analyses.

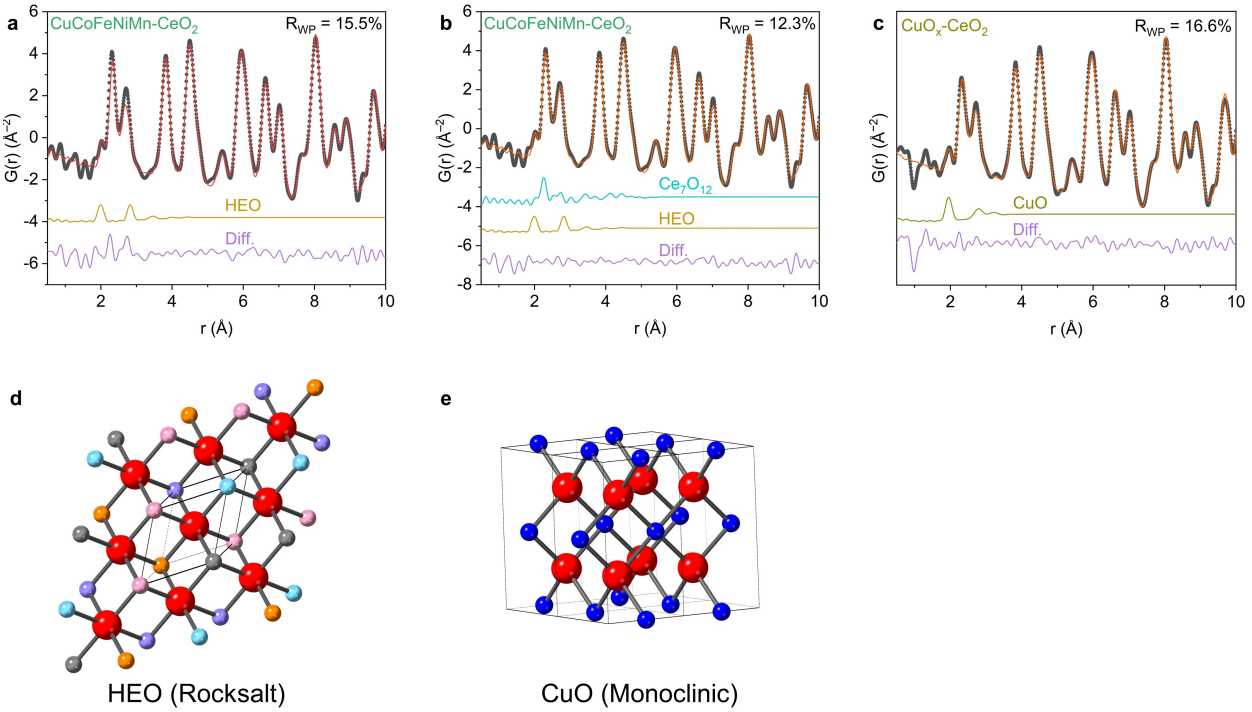

Figure S21. Short-range (0.5–10 Å) PDF analysis of CuCoFeNiMn-CeO_2 (a) excluding and (b) including the Ce_7O_{12} phase (Table S8). Based on the deconvoluted contribution, the domains size of the rocksalt HEO phase is less than 5 Å.[24] (c) Short-range (0.5–10 Å) PDF analysis of CuO_x-CeO_2 showing the monoclinic CuO domains. Schematics showing (d) the rocksalt HEO structure and (e) monoclinic structure for CuO.

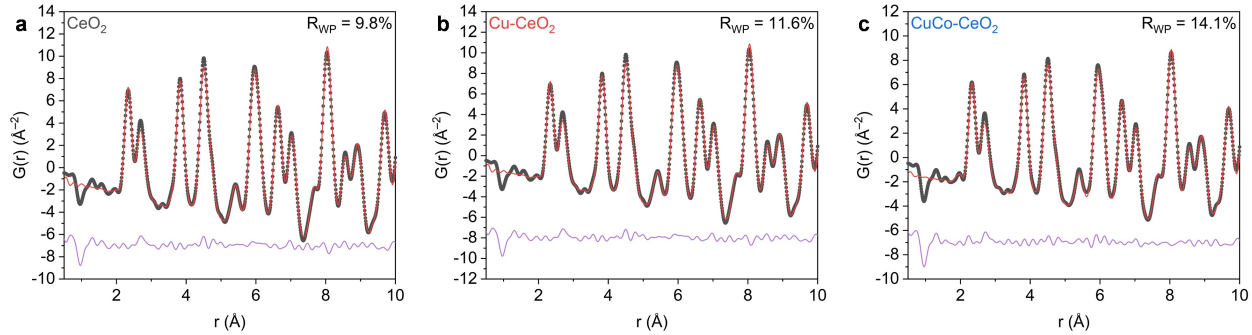

Figure S22. Short-range (0.5–10 Å) PDF analysis of (a) CeO_2, (b) Cu-CeO_2, and (c) CuCo-CeO_2 including the Ce_7O_{12} phase, and the fitting results are listed in Table S8. The negative peak at ~1 Å is due to the surface-adsorbed hydroxyl groups (–OH).

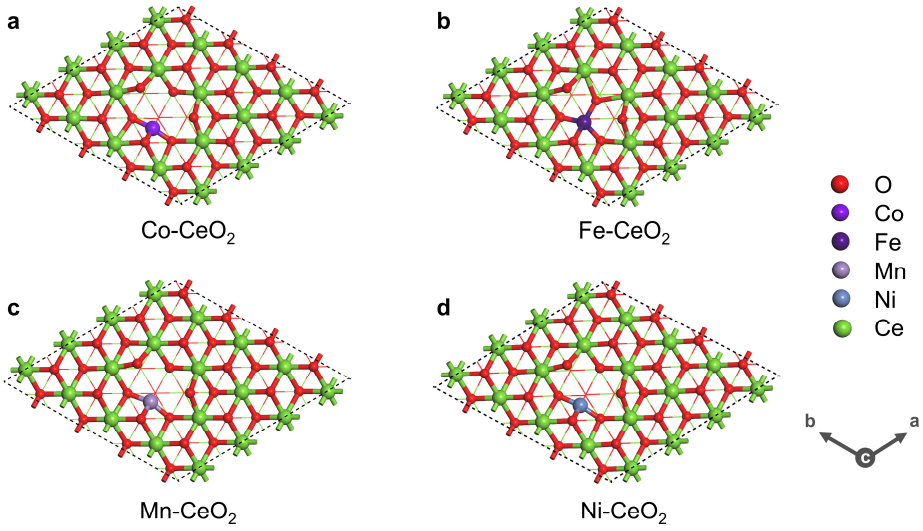

Figure S23. Optimized surface structures of (a) Co-CeO_2-(111), (b) Fe-CeO_2-(111), (c) Mn-CeO_2-(111), and (d) Mn-CeO_2-(111).

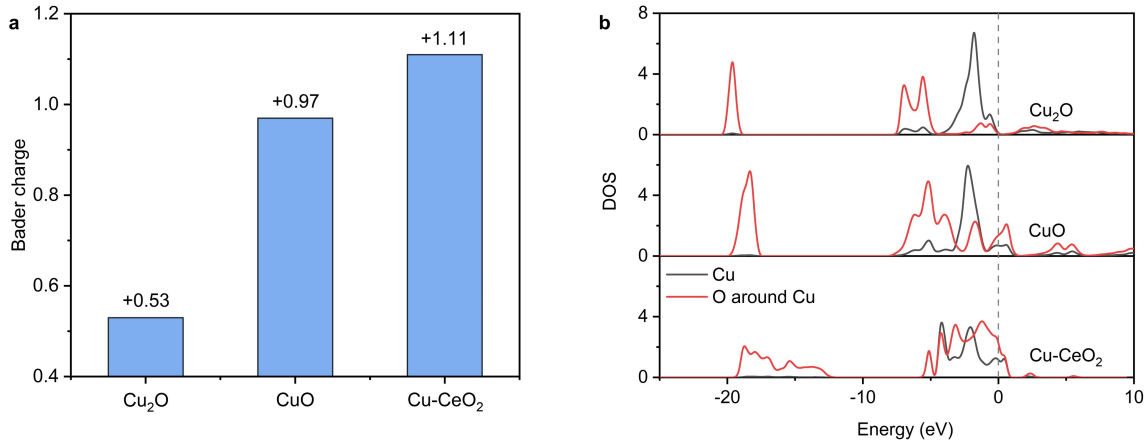

Figure S24. (a) Bader charge analysis of the copper atoms in Cu_2O, CuO and Cu-CeO_2, respectively, and (b) the corresponding calculated DOS of the copper and bonded oxygen atom. The Fermi level is noted using the dashed grey line.

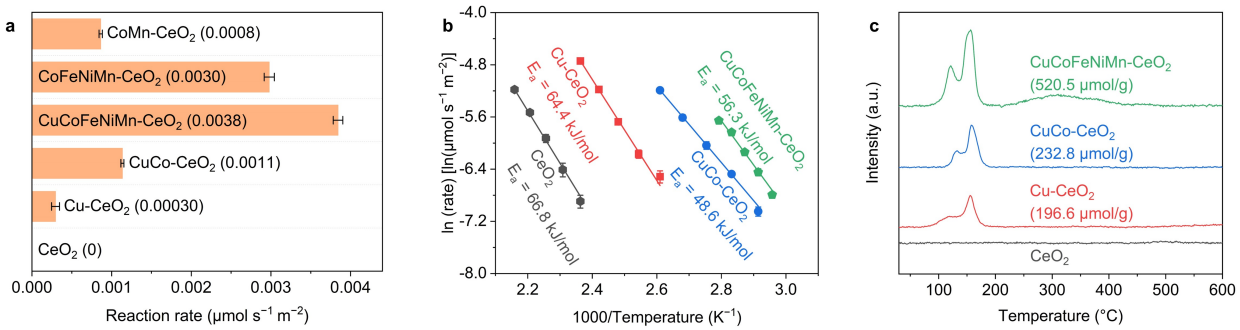

Figure S25. (a) Steady-state measurements of the CO oxidation reaction rates at 80 °C for CeO_2-based catalysts, with 20 mg catalysts in 1% CO balanced with dry air at a flow rate of 12 mL min^{-1}. (b) Arrhenius plots with apparent activation energies for the transition-metal-substituted CeO_2 samples, measured with 20 mg catalysts in 1% CO balanced with dry air at a flow rate of 12 mL min^{-1}. The conversion percentage was maintained below 15% by controlling the reaction temperature for kinetic studies, and the reaction rate was determined based on the average steady-state reaction rates in 1 h. (c) H_2-TPR profiles of the transition-metal-substituted CeO_2 catalysts with the H_2 consumption amount highlighted.

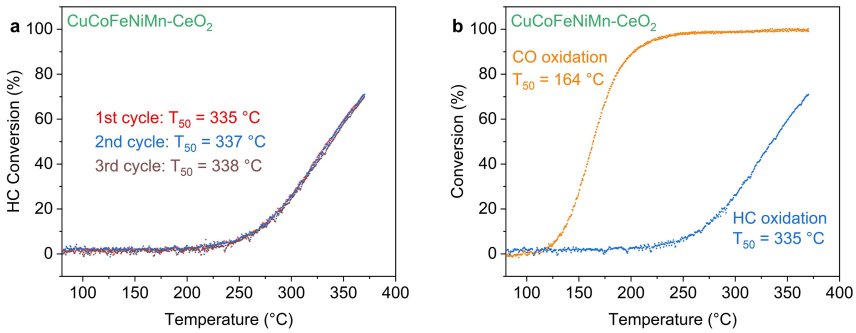

Figure S26. (a) Hydrocarbon (HC) oxidation light-off curves under simulated exhaust conditions for three repeated cycles. (b) Conversion of CO and hydrocarbons in the first catalytic cycle, indicating CO and hydrocarbons are converted at different temperature ranges.

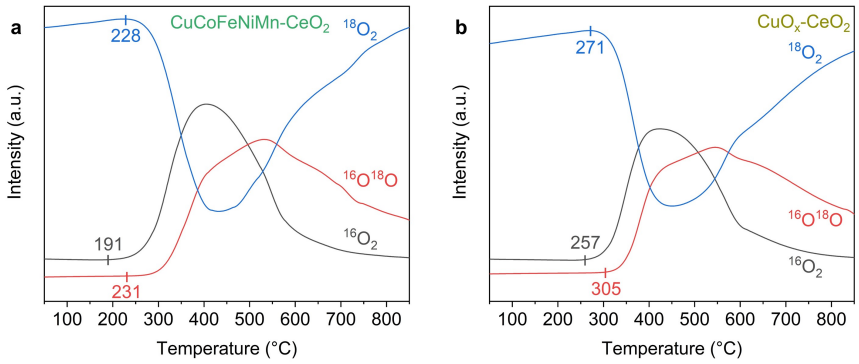

Figure S27. Evolution of the $^{16}O_2$, $^{16}O^{18}O$ and $^{18}O_2$ species for (a) CuCoFeNiMn-CeO_2 and (b) CuO_x-CeO_2 during the TPOIE measurement. The onset temperature is noted for comparison.

REFERENCES

(1) Lee, S. S.; Zhu, H.; Contreras, E. Q.; Prakash, A.; Puppala, H. L.; Colvin, V. L. High Temperature Decomposition of Cerium Precursors to Form Ceria Nanocrystal Libraries for Biological Applications. *Chem. Mater.* **2012**, *24*, 424–432.

(2) Brunauer, S.; Emmett, P. H.; Teller, E. Adsorption of Gases in Multimolecular Layers. *J. Am. Chem. Soc.* **1938**, *60*, 309–319.

(3) Heald, S. M.; Stern, E. A.; Brown, F. C.; Kim, K. H.; Barg, B.; Crozier, E. D. The PNC-CAT Insertion Device Beamline at the Advanced Photon Source. *Rev. Sci. Instrum.* **1996**, *67*, 3373–3374.

(4) Ravel, B.; Newville, M. ATHENA , ARTEMIS , HEPHAESTUS : Data Analysis for X-Ray Absorption Spectroscopy Using IFEFFIT. *J. Synchrotron Radiat.* **2005**, *12*, 537–541.

(5) Calvin, S. *XAFS for Everyone*; CRC press, **2013**.

(6) Mamontov, E.; Egami, T. Structural Defects in a Nano-Scale Powder of CeO2 Studied by Pulsed Neutron Diffraction. *J. Phys. Chem. Solids* **2000**, *61*, 1345–1356.

(7) Mamontov, E.; Egami, T.; Brezny, R.; Koranne, M.; Tyagi, S. Lattice Defects and Oxygen Storage Capacity of Nanocrystalline Ceria and Ceria-Zirconia. *J. Phys. Chem. B* **2000**, *104*, 11110–11116.

(8) Coelho, A. A.; Chater, P. A.; Kern, A. Fast Synthesis and Refinement of the Atomic Pair Distribution Function. *J. Appl. Crystallogr.* **2015**, *48*, 869–875.

(9) Usher, T.-M.; Olds, D.; Liu, J.; Page, K. A Numerical Method for Deriving Shape Functions of Nanoparticles for Pair Distribution Function Refinements. *Acta Crystallogr. Sect. A Found. Adv.* **2018**, *74*, 322–331.

(10) Farrow, C. L.; Juhas, P.; Liu, J. W.; Bryndin, D.; Božin, E. S.; Bloch, J.; Proffen, T.; Billinge, S. J. L. PDFfit2 and PDFgui: Computer Programs for Studying Nanostructure in Crystals. *J. Phys. Condens. Matter* **2007**, *19*, 335219.

(11) Grimley, D. I.; Wright, A. C.; Sinclair, R. N. Neutron Scattering from Vitreous Silica IV. Time-of-Flight Diffraction. *J. Non. Cryst. Solids* **1990**, *119*, 49–64.

(12) Kresse, G.; Hafner, J. Ab Initio Molecular-Dynamics Simulation of the Liquid-Metal–Amorphous-Semiconductor Transition in Germanium. *Phys. Rev. B* **1994**, *49*, 14251–14269.

(13) Kresse, G.; Hafner, J. Ab Initio Molecular Dynamics for Liquid Metals. *Phys. Rev. B* **1993**, *47*, 558–561.

(14) Blöchl, P. E. Projector Augmented-Wave Method. *Phys. Rev. B* **1994**, *50*, 17953–17979.

(15) Kresse, G.; Joubert, D. From Ultrasoft Pseudopotentials to the Projector Augmented-Wave Method. *Phys. Rev. B* **1999**, *59*, 1758–1775.

(16) Kresse, G.; Hafner, J. Ab Initio Molecular Dynamics for Open-Shell Transition Metals. *Phys. Rev. B* **1993**, *48*, 13115–13118.

(17) Perdew, J. P.; Burke, K.; Ernzerhof, M. Generalized Gradient Approximation Made Simple. *Phys. Rev. Lett.* **1996**, *77*, 3865–3868.

(18) Hautier, G.; Ong, S. P.; Jain, A.; Moore, C. J.; Ceder, G. Accuracy of Density Functional Theory in Predicting Formation Energies of Ternary Oxides from Binary Oxides and Its Implication on Phase Stability. *Phys. Rev. B* **2012**, *85*, 155208.

(19) Jain, A.; Hautier, G.; Moore, C. J.; Ping Ong, S.; Fischer, C. C.; Mueller, T.; Persson, K. A.; Ceder, G. A High-Throughput Infrastructure for Density Functional Theory Calculations. *Comput. Mater. Sci.* **2011**, *50*, 2295–2310.

(20) Elias, J. S.; Stoerzinger, K. A.; Hong, W. T.; Risch, M.; Giordano, L.; Mansour, A. N.; Shao-Horn, Y. In Situ Spectroscopy and Mechanistic Insights into CO Oxidation on Transition-Metal-Substituted Ceria Nanoparticles. *ACS Catal.* **2017**, *7*, 6843–6857.

(21) Dronskowski, R.; Bloechl, P. E. Crystal Orbital Hamilton Populations (COHP): Energy-Resolved Visualization of Chemical Bonding in Solids Based on Density-Functional Calculations. *J. Phys. Chem.* **1993**, *97*, 8617–8624.

(22) Maintz, S.; Deringer, V. L.; Tchougréeff, A. L.; Dronskowski, R. LOBSTER: A Tool to Extract Chemical Bonding from Plane-Wave Based DFT. *J. Comput. Chem.* **2016**, *37*, 1030–1035.

(23) Binder, A. J.; Toops, T. J.; Parks, J. E. II. Copper–Cobalt–Cerium Ternary Oxide as an Additive to a Conventional Platinum-Group-Metal Catalyst for Automotive Exhaust CatalysisLong-Range Antiferromagnetic Order in a Rocksalt High Entropy Oxide. *ChemCatChem* **2018**, *10*, 1263–1266.

(24) Zhang, J.; Yan, J.; Calder, S.; Zheng, Q.; McGuire, M. A.; Abernathy, D. L.; Ren, Y.; Lapidus, S. H.; Page, K.; Zheng, H.; Freeland, J. W. Budai, J. D.; Hermann, R. P. Long-Range Antiferromagnetic Order in a Rocksalt High Entropy Oxide. *Chem. Mater.* **2019**, *31*, 3705–3711.

(25) Huang, W. J.; Sun, R.; Tao, J.; Menard, L. D.; Nuzzo, R. G.; Zuo, J. M. Coordination-Dependent Surface Atomic Contraction in Nanocrystals Revealed by Coherent Diffraction. *Nat. Mater.* **2008**, *7*, 308–313.

(26) Wilkens, H.; Schuckmann, O.; Oelke, R.; Gevers, S.; Schaefer, A.; Bäumer, M.; Zoellner, M. H.; Schroeder, T.; Wollschläger, J. Stabilization of the Ceria ι-Phase (Ce_7O_{12}) Surface on Si(111). *Appl. Phys. Lett.* **2013**, *102*, 111602.

(27) Cargnello, M.; Chen, C.; Diroll, B. T.; Doan-Nguyen, V. V. T.; Gorte, R. J.; Murray, C. B. Efficient Removal of Organic Ligands from Supported Nanocrystals by Fast Thermal Annealing Enables Catalytic Studies on Well-Defined Active Phases. *J. Am. Chem. Soc.* **2015**, *137*, 6906–6911.

(28) Kümmerle, E. A.; Heger, G. The Structures of C–$Ce_2O_{3+\delta}$, Ce_7O_{12}, and $Ce_{11}O_{20}$. *J. Solid State Chem.* **1999**, *147*, 485–500.